A Versatile High Speed 250-MHz Pulse Imager for Biomedical Applications

BORIS EPEL, SUBRAMANIAN V. SUNDRAMOORTHY, COLIN MAILER, HOWARD J. HALPERN

Center for EPR Imaging In Vivo Physiology, Department of Radiation and Cellular Oncology, University of Chicago, Chicago, IL 60637

ABSTRACT: A versatile 250-MHz pulse electron paramagnetic resonance (EPR) instrument for imaging of small animals is presented. Flexible design of the imager hardware and software makes it possible to use virtually any pulse EPR imaging modality. A fast pulse generation and data acquisition system based on general purpose PCI boards performs measurements with minimal additional delays. Careful design of receiver protection circuitry allowed us to achieve very high sensitivity of the instrument. In this article, we demonstrate the ability of the instrument to obtain three-dimensional (3D) images using the electron spin echo (ESE) and single-point imaging (SPI) methods. In a phantom that contains a 1 mM solution of narrow line (16 μT, peak-to-peak) paramagnetic spin probe, we achieved an acquisition time of 32 s per image with a fast 3D ESE imaging protocol. Using an 18-min 3D phase relaxation (T_{2e}) ESE imaging protocol in a homogeneous sample, a spatial resolution of 1.4 mm and a standard deviation of T_{2e} of 8.5% were achieved. When applied to in vivo imaging this precision of T_{2e} determination would be equivalent to 2 Torr resolution of oxygen partial pressure in animal tissues. Concepts Magn Reson Part B (Magn Reson Engineering) 33B: 163–176, 2008

KEY WORDS: EPR imaging; low field EPRI; EPRI in vivo system design; phase relaxation; oxygen concentration

INTRODUCTION

Knowledge of the distribution of oxygen concentrations in tissues is of great interest in medicine, especially in tumor radiation therapy and chemotherapy (*1–3*) and heart disease (*4*). Therefore, several methods that can provide information about partial oxygen pressure, pO_2, have been investigated including reductive retention of positron emission radiotracer (*5*, *6*), Overhauser magnetic resonance imaging (*7*, *8*), and ^{19}F MRI (*9*). Electron Paramagnetic Resonance Imaging (EPRI) provides a fast and noninvasive method for the measurement of pO_2 in tissues using a spin probe exogenously administered to the animal (*10–16*). In this article, we apply three-dimensional (3D) pulse EPRI methodologies for in vivo imaging at 250 MHz, frequency low enough for application to human-size animals.

Although the basic principles of in vivo EPRI are very similar to the principles of nuclear Magnetic Resonance Imaging (MRI), the methodology of EPRI is considerably different from the conventional MRI due to the five to six orders of magnitude reduction in phase (T_{2e}) and spin-lattice (T_{1e}) relaxation times of the spin probes. This makes impossible the application of pulsed magnetic field gradients for imaging macroscopic objects, including living species. Micro-

Received 31 March 2008; revised 19 May 2008; accepted 22 May 2008

Correspondence to: Boris Epel; E-mail: bepel@uchicago.edu or Howard Halpern; E-mail: h-halpern@uchicago.edu

Concepts in Magnetic Resonance Part B (Magnetic Resonance Engineering), Vol. 33B(3) 163–176 (2008)

Published online in Wiley InterScience (www.interscience.wiley.com). DOI 10.1002/cmr.b.20119

scopic objects can be imaged using pulse gradients, for a recent example see (*17*).

Application of static magnetic field gradients ("gradients") allows the use of multiple EPRI modalities. Current EPRI applications are dominated by continuous wave (CW) imaging, which appears to be the most flexible modality considering the simplicity of the equipment and the broad variety of spin probes it can use. Conventional CW imaging is based on the filtered back projection reconstruction algorithm (FBP). Magnetic field swept spectra in the presence of gradients are acquired. The gradient directions and/or amplitudes are changed and the process repeated until the number of projections sufficient for image reconstruction is acquired. For a determination of pO_2, a spectral-spatial spectroscopic image can be obtained (*18*). The oxygen concentration is measured from the linear relation between pO_2 and the spin-packet line width. The spin-packet line width is obtained by fitting the fourth (spectroscopic) dimension of the 4D spectral-spatial image (*19*). The disadvantage of CW imaging is its relatively slow acquisition speed because the EPR spectrum acquisition requires the magnetic field to be swept. Since magnetic field coils typically have a large inductance, the imaging time is dependent on the maximum achievable magnetic field sweep rate. At present, in our 250-MHz CW EPRI instrument (*11*) the time for one scan of magnetic field is from 0.3 to 1 s. In our laboratory, a spectral-spatial CW image of a living animal limb takes about 45 min to acquire. This time is on the order of the clearance time of spin probes from tumors in the living organism and, therefore, can limit the use of CW imaging for time-critical biological applications.

Recently, there has been increasing interest in developing alternative fast EPRI techniques, such as spinning gradient EPRI (*20*), rapid scan (*21*), saturation CW imaging (*22*) as well as pulse imaging. In the pulse methodology, the EPR spectrum can be acquired in a time comparable to the T_{1e} of the spin probe. Most spin probes used for pulse imaging have T_{1e} of the order a few microseconds. Even taking into account that for reasonable SNR the acquisition and averaging of 1,000 or more measurements is required, a faster acquisition time than CW EPRI seems possible, i.e., milliseconds rather than seconds. The straightforward approach of using pulsed free induction decay (FID) imaging (*23*) was found to be not very successful at low frequencies since the T_{2e}^{*} of most spin probes is comparable with the "dead time" of EPR imagers. Truncation of FID time traces leads to serious artifacts in the obtained projections. To overcome imager "dead time" problems, a single-point imaging methodology (SPI) has been applied to EPR imaging (*24*). In the simplest form a single point on the FID at a known time, t_p, is recorded as a function of stepped gradient amplitudes sampled on a cubic grid. This signal forms a 3D "pseudo-echo," the FT of which generates a spatial image. The spatial information is encoded into the phase of FID. The relaxation times are extracted from multiple images obtained at different t_p. Because no information prior to t_p is required, SPI has no artifacts caused by the "dead time." Despite being the most artifact-free low frequency pulse EPR imaging methodology SPI has some disadvantages, the primary one of which is the acquisition time. A high resolution 3D SPI image (e.g., $100 \times 100 \times 100$) requires almost a half million measurements, each in the presence of a different gradient (see the Materials and Methods section). Analogous to the MRI spin echo experiment (*25*, *26*), a number of laboratories have developed electron spin echo imaging (ESE) at high frequencies (*27–30*). Mailer et al. demonstrated accurate oxygen images using 3D time-domain ESE imaging at 250 MHz (*31*). The application of this modality to living animals was presented briefly elsewhere (*32*). Time-domain ESE requires a considerably smaller number of measurements than SPI and accurately and directly measures T_{2e}. As a drawback, because this method is based on the FBP algorithm, it requires application of somewhat higher gradients for the comparable with SPI spatial resolution. The details of the ESE imaging modality will be described in the Materials and Methods section.

From the above, it is clear that there is no single imaging method that can satisfy all experimental needs of in vivo imaging. Therefore, a versatile instrument that can easily switch between different imaging techniques is essential. An important requirement for such an instrument is a minimum imaging time. Therefore, it has to have high signal-to-noise ratio (SNR) and exhibit an efficient control of devices and data acquisition. Although a number of low frequency instruments for in vivo imaging exist, see e.g., (*21*, *31*), none of them satisfies all of our requirements.

In this article, we present the salient technical features of our redesigned 250-MHz pulse EPR instrument for the imaging of small animals. This flexible imager executes virtually any pulse EPR imaging experiment with a high SNR and excellent performance of the pulse forming and data acquisition systems. We demonstrate the performance of this instrument in ESE and SPI imaging experiments. For the ESE method, we present promising acquisition strategies, enabled by high-speed data acquisition.

MATERIALS AND METHODS

Spin Probe and the Phantom

The spin probe used for the EPR imaging was a 1 mM solution of OX063H radical (methyl-tris[8-carboxy-2,2,6,6-tetrakis[(2-hydroxyethyl]benzo[1,2-d:4,5-d′]bis[1,3]dithiol-4-yl]-trisodium salt, molecular weight = 1,427 from GE Healthcare. This probe is a pharmaceutical grade MR contrast agent. The spin probe was contained in a flat-bottomed borosilicate glass cylinder of 9.5 mm inner diameter and 45 mm length. The sample was deoxygenated using a multiple-cycle freeze-pump-thaw technique and flame-sealed. The sample was placed into the resonator horizontally, along the resonator's axis of symmetry and centered in the axial plane of the resonator. Because the sample was half-full, this produced a meniscus at the liquid–air contact surface. The volume and concentration of the sample are similar to those in mice during EPR oxygen imaging experiments (*14*).

Pulse EPR Imager

Figure 1 shows a schematic drawing of our time-domain EPRI system operating at 250 MHz (magnetic field ~9 mT). The imager has a four coil air-core magnet with 4th order field compensation and Anderson-type *X*-, *Y*-, and *Z*-gradient coils (*33*, *34*). A B-MN 3× ± 40/60 C5 (Bruker BioSpin Corporation, Billerica, MA 01821-3991) linear current supply was used to drive the main coil and the *X*- and *Y*-gradients. The *Z*-gradient coil was driven by a BOP 50-20MG (KEPCO, Flushing, NY 11355) switching mode current supply. Quine et al. originally built the RF bridge of the imager according to the design of a 250 MHz homodyne pulse EPR spectrometer for relaxation measurements (*35*). Here, we present a greatly modified version of this bridge tailored to enhance performance for the purposes of in vivo imaging. Modifications include the use of a different resonator operated in reflection mode; a new transmit/receive (T/R) switch capable of interfacing with the reflection type resonators; an optimized design of the pulse arm and DC coupled video amplifiers. Additionally, we constructed a new data acquisition and gradient control system.

The reference frequency was generated by a HP8662A RF generator {1}. Here numbers in braces that follow the device name refer to the part numbers in Fig. 1. The output power of 1.3 mW divides equally between the pulse and the reference arms of the RF bridge. The low-power part of the pulse arm of the imager includes a digitally controlled Pulsar phase shifter {3}, a Mini-Circuits RF amplifier {4}, a Mini-Circuits switch {5}, and a high pass filter {6}. These components allowed us to generate RF pulses with rise and fall times better than 8 ns and phase controlled in 90° ± 5° steps. The manual rotary step-attenuator that controlled the pulse power {7} was placed before the power amplifier. The two-stage high power linear RF amplifier {8} (240–260 MHz, maximum power in the linear regime—2 kW, 2% maximum duty cycle) manufactured by Tomco Technologies, Norwood SA, Australia (*36*) was used to amplify pulses to ~1 kW peak power. The 10 dB fixed attenuator {9} on the output of the amplifier reduced the power to 100 W (maximum power was restricted by the power rating of components following the amplifier output). These amplified RF pulses had rise and fall times of ~12 ns. The gate of the amplifier's high power stage was controlled externally. The leading edge of the gate pulse preceded the RF excitation pulse by 325 ns. To reduce the switching noise of the preamplifier the preamplifier was not gated, i.e., it was always on. The amplifier has noise blanking that reduces the amplifier noise to within 20 dB above Johnson noise in less than 100 ns after the trailing edge of the RF pulse.

Unlike our earlier instrument in which we employed a bimodal cross-loop resonator (*31*, *37*), in this work we used a reflection mode single-loop single-gap resonator (LGR) consisting of a cylindrical inductive sample holding element (16 mm diameter, 15 mm long) with a single bridged capacitive element (*11*). The resonant structure was fabricated from ABS (acetonitrile-butadiene-styrene) plastic that has a good dimensional stability and can be easily plated. Conducting surfaces were fabricated by accurate plating of 12.5 μm silver (~3 skin depths at 250 MHz) and a 2-μm flash of gold for protection. The plating was provided by the facility in the laboratory of Prof. Eugenijus Norkus at the Department of Catalysis, Institute of Chemistry, University of Vilnius, Vilnius Lithuania as a kind gift. For the fine adjustment of resonator frequency, we added a non-magnetic 1–30 pf variable capacitor Johanson 5601 (Johanson Manufacturing Corporation, Boonton, NJ 07005) connected in parallel with the resonator's capacitive gap. The open structure of the LGR allowed easy access to the inner volume, which is useful for good animal placement. The quality factor, *Q*, of the empty resonator was 280 but for pulse experiments the loaded quality factor was reduced to 17 using a shunting resistor of 750 Ohms across the resonator's gap. The cavity was critically coupled to avoid a high level of reflections that can impair the detection system. A very important advantage of the

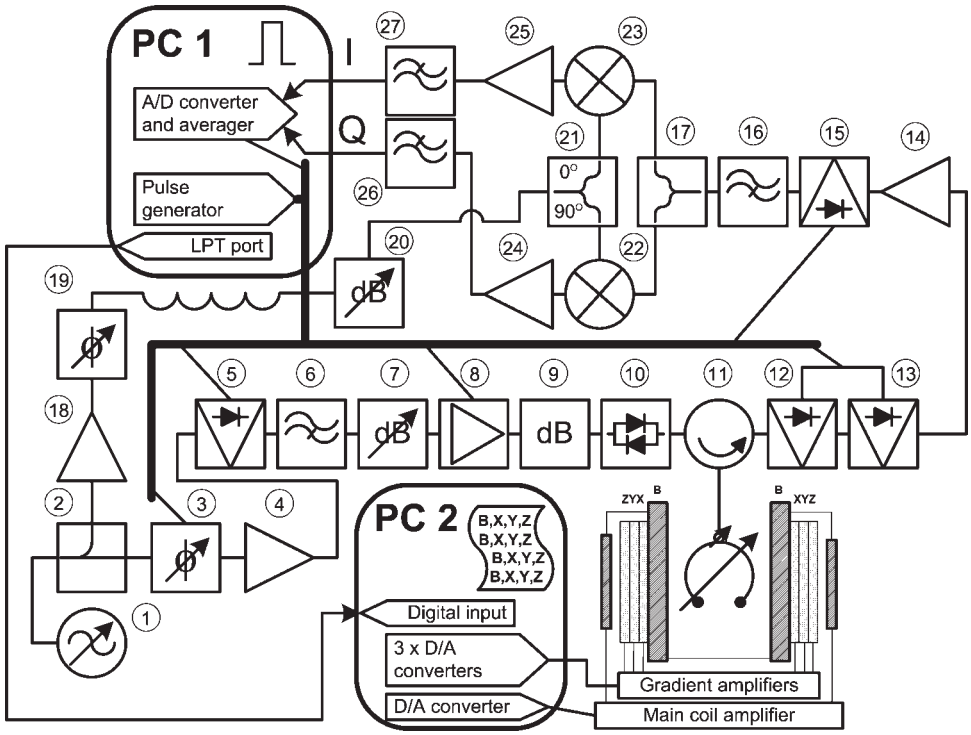

Figure 1 A block diagram of the pulse EPR imager. The bold line represents the pulse channels of the pulse generator. 1, HP8662A source (Agilent Technologies, Santa Clara, CA 95051); 2, ZMSC-2-1 power splitter (Mini-Circuits, Brooklyn, NY 11235); 3, MO-B2-412 phase shifter (Pulsar Microwave Corporation, Clifton, NJ 07012); 4, Mini-Circuits ZFL-500 amplifier; 5, Mini-Circuits ZASWA-2-50DR switch; 6, Mini-Circuits SHP-100 filter; 7, 50CAL10 0-10dB adjustable attenuator (Alan Industries, Columbus, IN 47201) and P/N 50DR-046 rotary step-attenuator (JFW Industries, Indianapolis, IN 46237); 8, 2 kW power amplifier (Tomco Technologies, Norwood, SA 5067, Australia); 9, Mini-Circuits CAT-10 attenuator; 10, cross-coupled diodes 1N4151; 11, 3A2BC circulator (Renaissance Electronics Corporation, Harvard, MA 01451); 12, HMC546MS8G switch (Hittite Microwave Corporation, Chelmsford, MA 01824); 13, Mini-Circuits ZYSWA-2-50DR switch; 14a, P240-270VDG low noise amplifier (Advance Receiver Research, Burlington CT 06013); 14b, 250GT low-noise amplifier (Anglelinear, Lomita, CA 90717-0035); 14c, AU-1A-0150 amplifier (MITEQ, Hauppauge, NY 11788); 15, Mini-Circuits ZYSWA-2-50DR; 16, Mini-Circuits SHP-100 filter; 17, Mini-Circuits ZFSC-2-1 splitter; 18, MITEQ AUP-1479 amplifier; 19, Pulsar MO-B2-412 quadrature phase shifter and Sage 6709 mechanical variable phase shifters (Sage Laboratories, NH 03051); 20, Alan Industries 50CAL10 0-10dB adjustable attenuator; 21, QHM-6-165 90° hybrid splitter (Merrimac, West Caldwell, NJ 07006); 22, 23, AD831-EB multipliers (Analog Devices, Norwood, MA 02062); 24, 25, homemade video amplifiers; 26, 27, Mini-Circuits BBLP-39 low pass filter.

LGR is its very high power conversion factor $B_1/\sqrt{W}$ so that an RF power of only 50 W was required for the 35 ns $\pi/2$- and 70 ns π-pulses needed for echo generation. A broadband high-isolation-low-insertion loss transmit/receive (T/R) switch whose overall isolation exceeded 110 dB was designed for use with this resonator. A Renaissance 3A2BC circulator {11} was used to direct power to and from the resonator. This circulator has a sufficient bandwidth (220–400 MHz) to pass RF pulses as short as 20 ns with minimal distortion and reflections (an RF pulse of 20 ns has an approximate bandwidth of 50 MHz). Our previous attempts to use circulators with narrower bandwidths (e.g., less than 30 MHz) failed due to the high level of reflections found. The Renaissance RF circulator, along with a high power Hittite switch (capable of handling up to 10 W power, failsafe) {12} and a high isolation Mini-Circuits switch {13} have together only 2.6 dB of insertion loss. The circulator itself is a source of a spurious signal, comparable with the signal of our typical samples. The two pulse EPR sequence generated a narrow distinc-

tive "echo" from the circulator. With the increase of delay between pulses this spurious echo intensity decreased with a characteristic decay time of about 400 ns. This signal was very stable and thus was easily corrected by the baseline subtraction. It did, however, limit the dynamic range of the imager. The true dead time of the imager was about 280 ns, however due to the circulator "echo" the protection switch was opened only after 350 ns after the last pulse. The bandwidth of the low noise (0.5 dB NF) amplifier (LNA) from Advance Receiver Research {14a} was 30 MHz. The components of the T/R switch, the LNA and the second stage RF amplifier were housed in a separate case and placed close to the resonator. The EPR signal (further amplified by two broadband single-stage amplifiers {14b} and {14c}) was demodulated using Analog Devices multipliers {22, 23} and fed into custom built DC coupled 20 MHz bandwidth video amplifiers {24, 25} with selectable gains from 34 to 54 dB. The signals were then filtered by low pass filters {26, 27} and digitized by fast analog-to-digital converters.

Imager Control and Data Acquisition. The imaging experiment was controlled by two standard PC stations operated under Windows XP (Microsoft Corporation, Redmond, WA 98052). The pulse console computer (Fig. 1, PC 1) contained a PulseBlasterESR pulse programmer (SpinCore Technologies, Gainesville, FL 32606; 21 channels, 2.5 ns resolution, 2.5 ns minimum pulse, and 12.5 ns minimum delay duration), an Acqiris AP235 ADC board equipped with 24 Mbytes of memory (Agilent Technologies, Monroe, NY 10950-1430; 2 channels, 8 bit ADC resolution, 2 ns minimum dwell time in a 2 channel configuration; phase-locked to the HP8662A source) and a PCI-GPIB board (National Instruments, Austin, TX 78759) for interfacing with the HP8662A RF source {1}. The pulse programmer controlled the phase of the phase shifter {3}, triggered the RF pulse switch {5}, the gate of the power amplifier {8}, the protection switches {12, 13, and 15}, and triggered the ADC board. The repetition rate of the experiment was controlled by the PulseBlasterESR unit.

The front-end program of the pulse console, SpecMan4EPR (www.specman4epr.com), is multipurpose pulse EPR software, which can generate arbitrary pulse sequences using a variety of third party devices (*38*). The magnetic field and gradients were controlled from another computer, PC 2, under control of a home-written program that uses the Labview™ environment (*32*). CW imaging in our laboratory is performed using the same software. The analog signals to drive the magnetic field and the linear current gradient amplifiers were generated using a PCI-6733 16-bit DAC board (National Instruments, Austin, TX 78759). PC 1 and PC 2 stations were synchronized using handshake protocol organized between the printer port LPT-1 of PC 1 and the digital I/O port of PCI-6289 board housed in PC 2. The sequence of gradients and magnetic fields was defined using look up tables loaded from a file generated prior to the experiment in MATLAB (The Mathworks, Natick, MA 01760).

ESE Imaging and Data Processing

ESE imaging protocol uses the protocol for 3D FBP reconstruction (*12*, *31*) and requires the acquisition of a number of projections with different orientations and fixed gradient amplitude, $|\vec{G}|$. The optimum gradient layout requires gradient directional vectors to be uniformly distributed on the surface of the unit hemisphere. The equal solid angle scheme (*39*) is very close to this layout. The overall number of projections required for the imaging is

$$N = \sum_{k=1}^{N_{\text{polar}}} \text{round}\left(N_{\text{az}} \sin\left(\frac{\pi}{2} + \frac{\pi}{N_{\text{polar}}}\left(k - \frac{1}{2}\right)\right)\right), \quad [1]$$

where N_{az} and N_{polar} are the maximum numbers of azimuthal and polar projections, respectively. round() is a function that rounds its argument toward nearest integer number. In the text, an image with N_{az} and N_{polar} projection is referred to as $N_{\text{az}} \times N_{\text{polar}}$. The number of projections derived from Eq. [1] reduces the total number of projections by $\sim$1/3. Thus, an equal solid angle 14 $\times$ 14 image requires 126 projections, whereas a 32 $\times$ 32 image requires 654 projections. For the reduction of FBP reconstruction artifacts, the original set of projections was four fold linearly interpolated to obtain a larger set of projections (*39*). These projections are filtered with a 3D Ram-Lak filter with a cutoff at 0.5 times the Nyquist frequency. The ESE images presented in this article were reconstructed using FBP code developed in our laboratory (*39*, *40*).

The ESE was detected using the two-pulse sequence $(\pi/2)_i - \tau - (\pi)_j - \tau -$ echo: here i and j indices denote the possible $\pm x$, $\pm y$ phases of the RF pulses and τ is the time delay between pulses. The $\pi/2$- and π-pulses had the same amplitude and durations of 35 and 70 ns, respectively. The applied RF power was optimized by maximizing the echo signal. A CYCLOPS 8-step phase cycling scheme (x, y; $-x$, y; x, $-y$; $-x$, $-y$; y, x; $-y$, x; y, $-x$; $-y$, $-x$) was

Table 1 Imaging Protocols

Protocol	Description
ESE-I	Two pulse echo sequence $(\pi/2) - \tau - (\pi) - \tau -$ echo; 35 ns $\pi/2$- and 70 ns π-pulses; $\tau = 0.63$ μs; 1,000 averages, including 8-step phase cycling, repetition time 15 μs; time domain trace 1,400 points, 4 ns dwell time; no baseline correction
ESE-Ia	The same like ESE-I except for five sequences with different τ logarithmically spaced between 0.63 and 2.4 μs are obtained
ESE-II	Two pulse echo sequence $(\pi/2) - \tau - (\pi) - \tau -$ echo; 35 ns $\pi/2$- and 70 ns π-pulses; $\tau = 0.63$ μs; 8,000 averages, including 8-step phase cycling, repetition time 15 μs; time domain trace 1,400 points, 4 ns dwell time; baseline correction every fourth trace (33 traces); FBP, equal solid angle 14×14 (126 projections), $\lvert\vec{G}\rvert = 10$ mT/m
ESE-IIa	The same as ESE-II except for five sequences with different τ logarithmically spaced between 0.63 μs and 2.4 μs are obtained
ESE-III	Two pulse echo sequence $(\pi/2) - \tau - (\pi) - \tau -$ echo; 35 ns $\pi/2$- and 70 ns π-pulses; $\tau = 0.63$ μs; 16,000 averages, including 8-step phase cycling, repetition time 15 μs; time domain trace 1,400 points, 4 ns dwell time; baseline correction every fourth trace (165 traces); FBP, equal solid angle 32×32 (654 projections), $\lvert\vec{G}\rvert = 15$ mT/m
ESE-IIIa	The same as ESE-III except for five sequences with different τ logarithmically spaced between 0.63 μs and 2.4 μs are obtained
SPI-I	FID detection using single $\pi/2$-pulse of 30 ns; 1,000 averages, including 4-step phase cycling correction, repetition time 7 us; time domain trace 400 points, 4 ns dwell time; no baseline correction
SPI-II	FID detection using single $\pi/2$-pulse of 30 ns; 16,000 averages, including 4-step phase cycling correction, repetition time 7 us; time domain trace 400 points, 4 ns dwell time; baseline correction for every ninth trace (113 traces); SPI, $11 \times 21 \times 11$ gradients grid restricted using $\lvert\vec{G}\rvert \leq G_{\max}$ inequality (1,007 projections), $\lvert\vec{G}_{\max}\rvert = 15$ mT/m, $t_p = 0.9$ μs

employed (unless mentioned separately). The sequence repetition time was 15 μs, and the shortest allowed by the duty cycle of the Tomco power amplifier. To obtain the image of phase relaxation five separate measurements with different τ delay values were performed. These delays have to cover the range of times suitable for correct determination of the relaxation time. For samples with a broad distribution of relaxation times (e.g., in a living organism), the precision of relaxation time determination was greater when these delays were spaced logarithmically. Consequently, ESE T_{2e} images were taken with τ spaced logarithmically between 0.63 and 2.4 μs.

All imaging protocols used in this work are summarized in Table 1. The ESE-I protocol demonstrates the basic timing of the technique. The "high speed" and "quality" protocols ESE-II and ESE-III include the gradient settling times and have off-resonance data collection for baseline subtraction. The "a" protocols are simply the multiple echo versions of ESE-II and ESE–III.

To avoid truncation artifacts due to the dead time of the imager, we used only the falling portions of the echoes rather than the full echo. The peaks of the echoes were fitted with Lorentzians for all projections separately. It was found experimentally that Lorentzian function provides the best approximation of the echo peak shape. The maximum of the statistical distribution of Lorentzian centers was taken as the ESE zero time for all traces. Phase correction using the two signals in quadrature was applied independently to every echo to maximize the real part of signal at zero time. The data were Fourier transformed (FT) to obtain spatial projections ready for inverse Radon transformation. Only the real part of Fourier transformed data was used for further reconstruction. These frequency projections were truncated using the relation: $\mathrm{FOV} = \gamma\lvert\vec{G}\rvert\Delta L$. Here FOV is the

field of view in MHz, $\gamma = 28.02$ MHz/mT is the electron gyro-magnetic ratio, and ΔL is the desired spatial field of view. All data processing was performed using script command files written in the MATLAB (The Mathworks, Natick, MA 01760) programming language.

Each set of projections recorded with different τ was reconstructed separately. A T_{2e} map was obtained by fitting the dependence of each image voxel amplitude on 2τ using the exponential decay function:

$$A(t) = A(0)\exp(-2\tau/T_{2e}). \quad [2]$$

Here $A(0)$ is the amplitude of the signal at $\tau = 0$ and T_{2e} is the phase relaxation time. Only voxels with signal amplitude above 20% of the maximum (from the image recorded with shortest τ) were used. The results were 3D spatial (i.e., amplitude at zero–time) and 3D T_{2e} images. For the analysis of the precision of the relaxation time determination the outer layer of voxels in the T_{2e} image was excluded from the statistics. For the pO_2 determination, the conversion coefficients for the OX063H radical from Ref. (*14*) were used.

SPI

The basic SPI technique is described elsewhere (*24*). The required FIDs were generated by 30 ns pulses with a repetition time of 7 μs. This pulse duration corresponds to a 71° Ernst angle for our spin probe with $T_{1e} = 6.2$ μs (*41*). The repetition rate was limited by the maximum allowed duty cycle of a power amplifier. Full CYCLOPS phase cycling was used. Gradients were generated on a 3D rectangular grid $11 \times 21 \times 11$. The number of projections is approximately equal to:

$$N \approx \frac{\pi}{6}\prod N_i, \quad [3]$$

where N_i are the three image dimensions. The coefficient of $\pi/6$ in Eq. [3] originates from the ratio of volumes between sphere and cube with equal diameter and side since measurements were performed only for the elements of the grid that satisfy the inequality $|\vec{G}| \leq G_{max}$. For the dimensions mentioned above, 1,007 gradients were sampled. The number of measurements can be further decreased by factor of one-half utilizing the symmetry relation between measurements with gradients $\vec{G}$ and $\vec{G}' = -\vec{G}$; however, we have found that this reduction negatively affects image quality. To produce an image, the $11 \times 21 \times 11$ experimental data were zero padded to obtain a $22 \times 42 \times 22$ matrix and Fourier transformed. No additional digital filters were applied.

Measurements and Algorithms

Main Coil and Gradient Coils Settling Times. The gradient and main field coils in any setup for in vivo imaging have considerable inductance and therefore substantial time is required to achieve the desired magnetic field in these coils. For linear current supplies, the settling time of a coil is approximately proportional to the magnetic field or gradient step (here expressed in seconds per Tesla or seconds per T/m). The settling time of our main DC field coil is 45 s/T. The settling times of *X*-, *Y*-, and *Z*-gradient coils are 0.6, 1.8, and 2.8 s*m/T, respectively.

For the SPI experiment with a gradient interval of ±15 mT/m and $11 \times 21 \times 11$ image dimensions the maximum gradient step is about 15 mT/m × 2/11 = 2.73 mT/m, which requires about 8 ms for the slowest *Z*-gradient coil. For ESE imaging with the same maximum gradient and a 14×14 protocol the gradient jump will be about 10 mT/m × 2/14 = 1.4 mT/m and will take about 4 ms (5 ms was used). To avoid gradient jumps higher than those described above, the gradient table was sorted into optimal order [see Ref. (*24*) for SPI and Ref. (*39*) for ESE]. For the baseline correction, traces were recorded with the magnetic field 0.9 mT lower than the resonance condition. To ensure that magnetic field had reached its equilibrium value we set a time of 100 ms to settle the off-resonance field step and 250 ms to settle once back on-resonance.

Receiver Arm Bandwidth. The bandwidth of the receiver arm of the imager was measured using a network analyzer HP8752ES (Agilent Technologies, Santa Clara, CA 95051). The excitation arm of the analyzer (output power of −35 dBm) attenuated by 40 dB was connected to the resonator port of the circulator {11}. The power arm port of the circulator was terminated with 50 Ohm. The Network analyzer was phase-locked to the HP8662A source {1}. The desired range of frequencies of the network analyzer was swept using computer control. The oscillatory time traces at each frequency value acquired by the Acqiris AP235 board (in single shot mode, trace length 4 μs) were Fourier transformed to obtain the signal amplitude and this, plotted versus frequency gave the dependence of signal amplitude on excitation frequency and hence the amplifiers bandwidth.

Imager Frequency Characteristic. To measure the cumulative imager profile, a 1 mM OX063H phantom was placed into the resonator and FIDs (for SPI) or spin echoes (for ESE) were recorded as a function of the stepped magnetic field and then Fourier trans-

formed. This gave the dependence of the FID and echo signal amplitudes and phases on magnetic field position. Because the natural inhomogeneous line width of the OX063H, 16 μT, is sufficient to produce an echo no imaging gradients were applied.

Measurement of T_{2e} and Spatial Resolution. The performance of ESE imaging was characterized by the T_{2e} and spatial resolution. For the measurement of the T_{2e} resolution, only voxels of the homogeneous phantom with amplitudes greater than 20% of the maximum were selected. We defined the T_{2e} resolution as the standard deviation of the T_{2e} from all of the voxels in the homogeneous phantom with one outer layer eroded. The spatial resolution of an image can be quantified by the response of an image to an abrupt step function change in sample density, viz., no sample at one side and constant sample density on the other side of the boundary of a homogeneous phantom (*40*). The change of image signal intensity obtained along a line perpendicular to this edge was fitted with the Gauss error function $\mathrm{erf}\left(x/\sigma\sqrt{2}\right)$. The width of this error function (σ) gives an estimate of the spatial resolution. The σ value is an average of 75 measurements distributed on the surface of the sample adjacent to the wall of the bottle. The spatial resolution of the ESE images was measured from an images obtained with $\tau = 0.63$ μs.

T_{2e} Measurements Under Non-Imaging Conditions. Phase relaxation time was measured using a two-pulse sequence. The $\pi/2$ and π pulses had the same amplitude and durations of 35 and 70 ns, respectively. Eight-step phase cycling was used and τ was varied from 0.63 to 20 μs (120 points logarithmically spaced). The repetition time was 80 μs. Gradients were not applied during the measurement. The falling portion of the echo was integrated to obtain the amplitude.

RESULTS AND DISCUSSION

Receiver Arm Bandwidth

The pulse imager acquires the complete signal line shape all-at-once, and therefore its receiver arm frequency bandwidth has to be sufficient to accommodate the whole spectrum of signal frequencies. The bandwidth of the receiving arm of the pulse bridge was measured to be about 37 MHz (see Fig. 2). This bandwidth should be in principle sufficiently flat to perform imaging of 3 cm cubic object with an applied gradient of up to 30 mT/m (0.03 m $\times \sqrt{3} \times$ 30 mT/m $\times$ 28.02 MHz/mT = 35.6 MHz) although in practice other factors limit the useful bandwidth—vide infra.

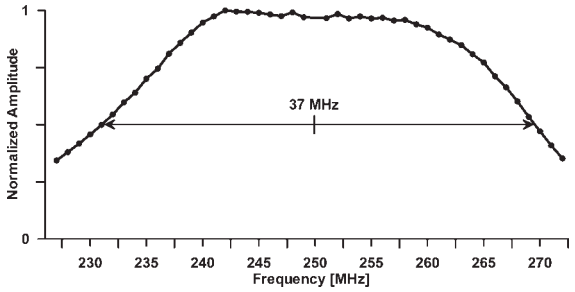

Figure 2 The imager receiver arm frequency response profile.

Frequency Profile Correction

The collective distortion of the signal frequency profile introduced by the imager is a complicated function of the receiver arm frequency response profile, the resonator bandwidth, and the frequency spectrum of applied RF pulses. One can significantly improve the quality of the image by correcting all the acquired projections using this function. Because the response of the spin system is not linear with power and RF pulses have a nonideal shape, it is very hard to calculate a correction function from the first principles. An alternative is to determine the function experimentally for a given instrument, the quality factor of the cavity (Q) and the duration of the RF pulses (t_p^i). An example of such a function for an ESE pulse sequence is presented in the Fig. 3. As one can see the cumulative profile (7.1 MHz) is considerably narrower than the bandwidth of the resonator (250 MHz/17 $\approx$ 14.7 MHz) and the pulses (1/70 ns $\approx$ 14 MHz, 1/35 ns $\approx$ 29 MHz). The cumulative bandwidth of the imager can be roughly estimated by the relation:

$$\mathrm{BW} \approx 1 \Big/ \left(\frac{1}{\mathrm{BW_R}} + \sum \frac{1}{\mathrm{BW_p^i}} \right) \approx 1 \Big/ \left(\frac{Q}{\nu} + \sum t_p^i \right) \approx 5.8 \text{ MHz.} \quad [4]$$

Here $\mathrm{BW_R}$ and $\mathrm{BW_p^i}$ are the bandwidths of resonator and RF pulses, respectively; ν is the imager frequency. The direct consequence of Eq. [4] is that for the SPI pulse sequence, which consists of a single 29 MHz-wide $\pi/2$-pulse, the cumulative bandwidth will be always broader than the ESE bandwidth. Using Eq. [4], we can estimate the largest possible bandwidth of our instrument to be about 19 MHz for ESE and 27 MHz for SPI. These estimates assume

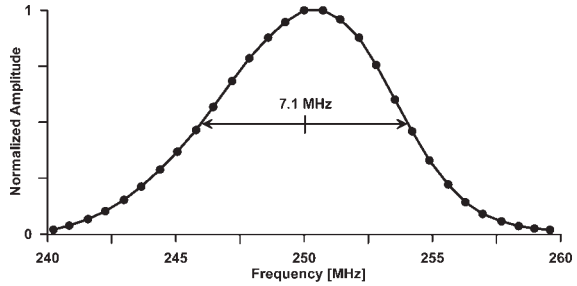

Figure 3 The cumulative frequency profile of the imager as determined using a two pulse echo signal. The profile was measured with the resonator Q set to 17 (equivalent bandwidth 14.7 MHz) and an ESE sequence with 35 and 70 ns $\pi/2$- and π-pulses (equivalent bandwidths of 28.6 and 14.3 MHz, respectively).

that the shortest RF pulses our instrument can generate are 16 ns and that the minimum feasible resonator Q is 5. These experiments will require RF power on the order of 1 kW. This power level is achievable by the power amplifier used but exceeds the maximum allowed power of the present receiver protection circuitry.

Baseline Correction

Considerable improvement of image quality was obtained when off-resonance time traces were subtracted from the on-resonance data traces. This procedure removed virtually all image artifacts due to RF reflections, circulator spurious "echoes" and resonator ring down. Figure 4 shows axial cross-section of the phantom. The meniscus can clearly be seen. However, it can be seen that the image reconstructed from projections corrected using just one baseline trace recorded prior to the experiment has an obvious "zero" artifact [marked by an arrow in Fig. 4(A)]. This artifact is independent of imaging modality and is located in the center of the image, at the point where all the gradients coincide with zero value. We believe that the major source of this artifact is ambient frequency pick-up. This is not surprising considering the high sensitivity of the instrument. We found that the best suppression of the "zero" artifact was achieved when off-resonance time traces were acquired immediately after every data trace. This mode of operation was very time consuming because of the amount of on-off field stepping involved. Therefore, we acquired off-resonance time traces less frequently and generated the missing off-resonance traces using cubic spline interpolation for every point of the time trace. It was found empirically that a baseline acquisition for every fourth trace was sufficient for a high quality ESE image [see Fig. 4(B)]. For SPI baseline acquisition every ninth trace was satisfactory.

Acquisition Speed

An image's overall acquisition time depends both on the imaging parameters (e.g., the number of projections, base line traces, averages, etc) and on the performance of the imager itself. The efficiency of an instrument can be characterized by the performance overhead—the excess of the actual experimental time over and above the "ideal" calculated data acquisition time (simply the total number of acquired traces times the repetition time per trace): Overhead $= (t_{\mathrm{exp}} - t_{\mathrm{ideal}})/t_{\mathrm{ideal}} \times 100\%$. The smaller the overhead the more efficiently the imager can acquire the data. The overhead of the imager results from the additional time necessary i) to send appropriate commands to the imager components and to transfer acquired data from analog to digital converters to the computer; ii) to settle the currents in the main field and gradient coils.

During the imaging, a number of different sequences are generated and corresponding data acquired as shown in Table 1. For the SPI pulse sequence, there are four phase cycle steps and for the ESE sequence, an eight-step phase cycle and five measurements with different τ (all together 40 different sequences). The pulse programmer (PulseBlasterESR) has an onboard memory sufficient to store about 500 different single-pulse or ESE sequences. The Acqiris ADC board has the capability to average multiple traces in a single programming cycle (up to 65,535 averages per trace). The board equipped with 24 Mbytes of onboard memory can store more than 500 time traces per channel, 2,000-points each. Therefore, all pulse sequences required for a particular gradient setting can be generated and acquired during one programming cycle. Phase cycling performs best when all steps of the phase cycling are done first in the inner cycle and, then, repeated a 'number-of-averages' times. For ESE, the optimal way is to place the phase cycling into the innermost cycle, change to different τ values in the intermediate cycle and average data in the outer cycle. Below we demonstrate that this mode of programming is favorable not only from the experimental point of view but considerably reduces the overhead. The timings for ESE and SPI pulse sequences with different phase cycling schemes are presented in the Tables 2 and 3. The data are given for the very fast imaging experiments ESE-I and SPI-I that have only 1,000 averages per projection and zero gradient settling time. The programming of all

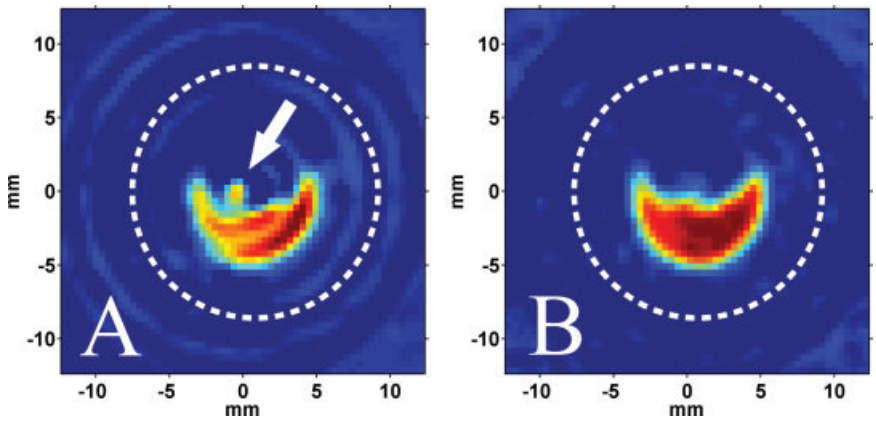

Figure 4 Influence of the baseline correction on the quality of image obtained with the ESE-III protocol. Images were reconstructed from the projections corrected using: one base line acquired prior to the experiment (A) and baselines acquired for every fourth projection (B). The area of the largest artifact [marked by the arrow in Fig. 4(A)] corresponds to the three gradients zero crossover point of the imager. An axial cross section of the phantom is presented.

sequences at once allows one to reduce the overhead time by a factor of 3–5 compared to separate programming. In addition, one can see that experiments with different phase cycling schemes have very little difference in performance overhead. All listed strategies are built into the SpecMan4EPR software.

Because of the limited SNR, the imaging protocols applied for in vivo imaging typically have a higher number of averages. The overhead of these protocols due to the factors described earlier will be smaller the larger the number of averages. For example, the overhead for the scheme with five 1,000-averages sequences (Table 3, sequences with different τ programmed at once) of 13% will decrease below 2% for measurements with 8,000 averages.

Examples

Figure 5 presents selected saggital slices of ESE and SPI 3D images of the homogeneous 1 mM OX063H. The white frame marks the boundary of the resonator. The bottom of the phantom is aligned with the left edge of the resonator so that the vial extends to

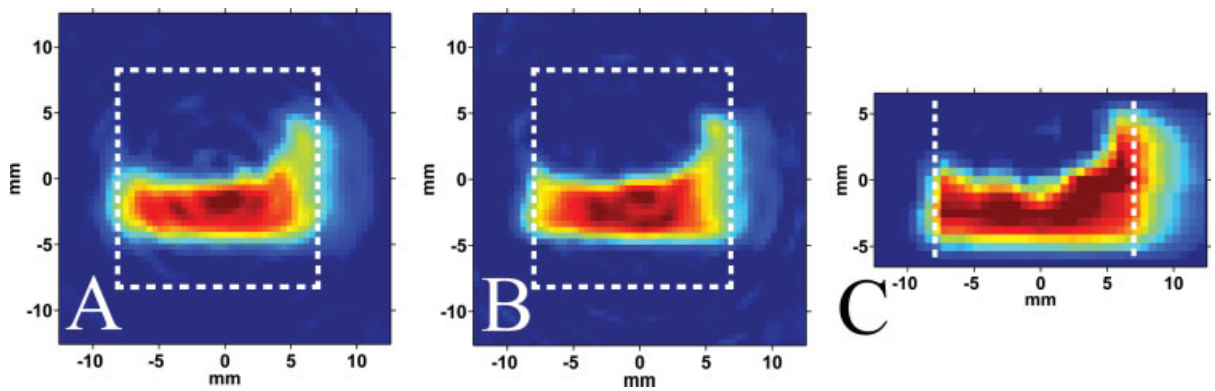

Figure 5 Selected saggital slices of 3D images of the homogeneous 1 mM OX063H phantom. The white frame marks the boundary of the resonator. The bottom of the phantom is aligned with the left edge of the resonator while the rest of the phantom extends to the right beyond the resonator sensitive volume. (A) "Fast" image obtained using the ESE-II protocol, imaging time 32 s. (B) "Quality" image obtained using the ESE-III protocol, imaging time 4 min 20 s. (C) SPI image obtained using the SPI-II protocol, imaging time 2 min 54 s.

Table 2 Dependence of the Single Projection Acquisition Time for Single τ ESE Imaging and SPI on the Number of Phase Cycles

Protocol	Acquisition Time (ms)	"Ideal" Imaging Time[a] (ms)	Overhead (%)
ESE-I, all phase cycling steps programmed at once			
8 steps	18	15	20
4 steps	18		20
2 steps	17		13
ESE-I, phase cycling steps programmed separately			
8 steps	26	15	73
1 step	17		13
SPI-I, all phase cycling steps programmed at once			
4 steps	8	7	14
SPI-I, phase cycling steps programmed separately			
4 steps	11	7	57
1 step	8		14

The acquisition times are averages obtained from 1,000 measurements.
[a] The "ideal" imaging time includes only the pure acquisition time.

the right beyond the resonator's right hand edge. The first two images [Figs. 5(A,B)] were obtained using ESE and their acquisition parameters are summarized in the Table 4. Acquisition times in these examples refer to the full acquisition time including overhead. The fast, 32 s acquisition time, ESE-II image in the Fig. 5(A) presents the capabilities of our instrument for rapid imaging. Because of a low number of projections this image contains minor artifacts and some amplitude nonuniformity. The decrease of the intensity toward the image edges is due to the magnetic field B_1 nonuniformity outside the resonator. The length of the resonator is 15 mm, correspondingly areas of the sample more than ± 7.5 mm from the center are located in the fringe field. The spatial resolution of the image is 2.0 mm. Significant improvement is observed in the "quality" image obtained using the 4 min 20 s long ESE-III protocol [Fig. 5(B)]. Because of the 50% higher gradient and five times more projections, the resolution of this image is substantially better—1.4 mm. The SPI image presented in the Fig. 5(C) has 1.4 mm resolution. The phase encoding protocol of the spin probe spatial distribution in SPI makes the resolution of an SPI image equal to the voxel size. Using the prior knowledge of the phantom and resonator dimensions, it is more efficient to use an asymmetric imaging procedure (11 steps along the *XZ* directions perpendicular to the long axis of resonator and 21 steps along the resonator *Y* axis). Thus, the SPI image in Fig. 5(C) is smaller in the vertical dimension. Nevertheless, the imaged region is sufficient to include the phantom completely. The results of the imaging of SPI and ESE are identical for the inner resonator volume, outlined by the frames in Figs. 5(A,B) and vertical lines in Fig. 5(C). One can notice that the SPI image is much more sensitive to the fringe fields. The right hand edge of our phantom extends far beyond the inner resonator volume on one side of the resonator (right side of the images in Fig. 5). The SPI image has considerable intensity out to 12.5 mm from the center of the resonator, 5 mm outside the physical dimensions of the resonator. In contrast, the ESE image intensity is negligible at 10 mm to the right from the resonator center, 2.5 mm from the right-hand edge of the resonator. The reason for this difference is that the ESE has stronger dependence of signal intensity on RF pulse turning angle than FID signal (*42*). The turning angle of an RF pulse is proportional to the strength of RF field that is highest in

Table 3 Dependence of the Acquisition Time for ESE Imaging on Programming Type

Protocol	Acquisition Time (ms)	"Ideal" Imaging Time (ms)	Overhead (%)
ESE-Ia, sequences with different τ programmed separately	135	75	80
ESE-Ia, sequences with different τ programmed at once	85		13

The acquisition times are averages obtained from 200 measurements.

Table 4 EPRI Protocols and Image Parameters

Protocol and Gradient	Projections/ Base Lines	"Ideal" Imaging Time	Imaging Time (Overhead)	Spatial Resolution, σ (mm)	Standard Deviation of T_{2e}
"Fast" ESE protocols					
ESE-II (spatial only)	126/33	19 s	32 s (30%)	2.0	
ESE-IIa (3D T_2 image)	126/33	1 min 35 s	1 min 48 s (15%)	2.0	0.76 μs
"Quality" ESE protocols					
ESE-III (spatial only)	654/165	3 min 17 s	4 min 20 s (32%)	1.4	
ESE-IIIa (3D T_2 image)	654/165	16 min 23 s	17 min 35 s (7%)	1.4	0.41 μs
SPI protocol					
SPI-II (spatial only)	1,007/113	2 min 05 s	2 min 54 s (39%)	1.4	

the inner volume of the resonator and gradually decreases outside resonator.

The distributions of the T_{2e} values obtained for the "fast," ESE-IIa, and the "quality," ESE-IIIa, ESE imaging protocols are presented in the Fig. 6. The means of both distributions (4.43 and 4.54 μs, for the "fast" and "quality" images, respectively) are not statistically different from the average T_{2e} of 4.8 μs measured in a nonimaging experiment. The standard deviations of T_{2e} of the "fast" and "quality" images were found to be 0.76 and 0.41 μs, respectively. The reduction in standard deviation can be attributed to the better SNR of the "quality" image. In terms of pO_2 these standard deviations result in 4 and 2 Torr precision, respectively.

The relaxation parameter that can be directly determined from SPI is T_{2e}^*. Besides the true T_{2e} that is dependent on oxygen concentration, the observed relaxation time has other contributions (see e.g., Ref. (*21*)). An elaborate calibration procedure is required to obtain pO_2 from an SPI image and as our aim was simply to demonstrate that we could efficiently obtain both SPI and ESE data in the same instrument, we did not determine the SPI derived pO_2 standard deviation in this work.

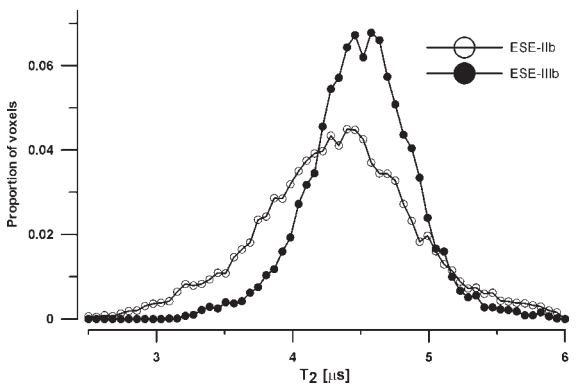

Figure 6 The distribution of T_{2e} in the image of the homogeneous 1 mM OX063H phantom obtained using 5-echo ESE imaging. "Fast" ESE-IIa image: imaging time 1 min 48 s, mean T_{2e} value 4.43 μs, standard T_{2e} deviation 0.76 μs. "Quality" ESE-IIIa image: imaging time 17 min 35 s, mean T_{2e} value 4.54 μs, standard T_{2e} deviation 0.41 μs.

The need to record the traces for baseline subtraction results in an increase of the experiment time. For example, the "quality" ESE-III protocol has a 63 s overhead arising from 654 gradient settling steps of 5 ms and 165 off-/on-resonance main field jumps of 350 ms duration, taking ~3.3 and 58 s, respectively. We are aiming for improvements to the imager's stability that should reduce the need to do such baseline corrections and consequently reduce the experiment time.

The overhead of the SPI-II protocol exceeds that for ESE-IIa and ESE-IIIa (see Table 4). Comparing this overhead with the SPI-I experimental overhead (see Table 2), we see that major contribution to overhead are gradient and, especially, field settling times. The large linear volume (a sphere of 150 mm diameter) gradient system of our magnet was designed for CW EPR imaging and has relatively high inductance and requires long settling times. An imager that has field and gradient coils with lower inductance will perform considerably faster. For example, an SPI imager equipped with high-performance MRI-type coils demonstrated a ~20% overhead in a similar experiment (*43*). From these results, we conclude that for imagers with slow, high inductance gradient coils, the ESE imaging protocols that contain less gradient steps are more efficient. Imagers with fast, low inductance field and gradient coils will perform equally well using either methodology.

CONCLUSIONS

The pulse EPR imager presented in this work satisfies all requirements of a modern instrument. It com-

bines high SNR and acquisition speed with versatility that allows the use of this instrument for different imaging modalities.

ACKNOWLEDGMENTS

We acknowledge our collaborators at the University of Denver, Dr. Gareth Eaton, Dr. George Rinard, and Mr. Richard Quine for valuable advice in numerous modifications of RF bridge and for helpful discussions of imaging problems. This work is supported by NIH, grants numbered P41 EB002034 and R01 CA98575.

REFERENCES

1. Hockel M, Schlenger K, Aral B, Mitze M, Schaffer U, Vaupel P. 1996. Association between tumor hypoxia and malignant progression in advanced cancer of the uterine cervix. Cancer Res 56:4509–4515.
2. Brizel DM, Rosner GL, Prosnitz LR, Dewhirst MW. 1995. Patterns and variability of tumor oxygenation in human soft-tissue sarcomas, cervical carcinomas, and lymph-node metastases. Int J Radiat Oncol Biol Phys 32:1121–1125.
3. Brizel DM, Sibley GS, Prosnitz LR, Scher RL, Dewhirst MW. 1997. Tumor hypoxia adversely affects the prognosis of carcinoma of the head and neck. Int J Radiat Oncol Biol Phys 38:285–289.
4. Kuppusamy P, Chzhan M, Wang PH, Zweier JL. 1996. Three-dimensional gated EPR imaging of the beating heart: time-resolved measurements of free radical distribution during the cardiac contractile cycle. Magn Reson Med 35:323–328.
5. Koh WJ, Rasey JS, Evans ML, Grierson JR, Lewellen TK, Graham MM, et al. 1992. Imaging of hypoxia in human tumors with [F-18] fluoromisonidazole. Int J Radiat Oncol Biol Phys 22:199–212.
6. Dehdashti F, Mintun MA, Lewis JS, Bradley J, Govindan R, Laforest R, et al. 2003. In vivo assessment of tumor hypoxia in lung cancer with Cu-60-ATSM. Eur J Nucl Med Mol Imaging 30:844–850.
7. Golman K, Petersson JS, Ardenkjaer-Larsen JH, Leunbach I, Wistrand LG, Ehnholm G, et al. 2000. Dynamic in vivo oxymetry using Overhauser enhanced MR imaging. J Magn Reson Imaging 12:929–938.
8. Krishna MC, English S, Yamada K, Yoo J, Murugesan R, Devasahayam N, et al. 2002. Overhauser enhanced magnetic resonance imaging for tumor oximetry: c4oregistration of tumor anatomy and tissue oxygen concentration. Proc Natl Acad Sci USA 99:2216–2221.
9. Mason RP, Shukla H, Antich PP. 1993. In vivo oxygen-tension and temperature—simultaneous determination using F-19 NMR-spectroscopy of perfluorocarbon. Magn Reson Med 29:296–302.
10. Berliner LJ, Fujii H. 1985. Magnetic-resonance imaging of biological specimens by electron-paramagnetic resonance of nitroxide spin labels. Science 227:517–519.
11. Halpern HJ, Spencer DP, Vanpolen J, Bowman MK, Nelson AC, Dowey EM, et al. 1989. Imaging radiofrequency electron-spin-resonance spectrometer with high-resolution and sensitivity for in vivo measurements. Rev Sci Instrum 60:1040–1050.
12. Eaton GR, Eaton SS, Ohno K. 1991. EPR Imaging and In Vivo EPR. Eaton GR, Eaton SS, Ohno K, editors. Boca Raton, FL: CRC Press.
13. Kuppusamy P, Chzhan M, Vij K, Shteynbuk M, Lefer DJ, Giannella E, et al. 1994. 3-Dimensional spectral spatial EPR imaging of free-radicals in the heart—a technique for imaging tissue metabolism and oxygenation. Proc Natl Acad Sci USA 91:3388–3392.
14. Elas M, Williams BB, Parasca A, Mailer C, Pelizzari CA, Lewis MA, et al. 2003. Quantitative tumor oxymetric images from 4D electron paramagnetic resonance imaging (EPRI): methodology and comparison with blood oxygen level-dependent (BOLD) MRI. Magn Reson Med 49:682–691.
15. Halpern HJ, Yu C, Peric M, Barth E, Grdina DJ, Teicher BA. 1994. Oxymetry deep in tissues with low-frequency electron paramagnetic resonance. Proc Natl Acad Sci USA 91:13047–13051.
16. Bratasz A, Pandian RP, Deng Y, Petryakov S, Grecula JC, Gupta N, et al. 2007. In vivo imaging of changes in tumor oxygenation during growth and after treatment. Magn Reson Med 57:950–959.
17. Blank A, Freed JH, Kumar NP, Wang CH. 2006. Electron spin resonance microscopy applied to the study of controlled drug release. J Controlled Release 111:174–184.
18. Maltempo MM, Eaton SS, Eaton GR. 1987. Spectral-spatial two-dimensional electron-paramagnetic-res imaging. J Magn Reson 72:449–455.
19. Mailer C, Robinson BH, Williams BB, Halpern HJ. 2003. Spectral fitting: the extraction of crucial information from a spectrum and a spectral image. Magn Reson Med 49:1175–1180.
20. Ohno K, Watanabe M. 2000. Electron paramagnetic resonance imaging using magnetic-field-gradient spinning. J Magn Reson 143:274–279.
21. Subramanian S, Koscielniak JW, Devasahayam N, Pursley RH, Pohida TJ, Krishna MC. 2007. A new strategy for fast radiofrequency CW EPR imaging: direct detection with rapid scan and rotating gradients. J Magn Reson 186:212–219.
22. Hama Y, Matsumoto KI, Murugesan R, Subramanian S, Devasahayam N, Koscielniak JW, et al. 2007. Continuous wave EPR oximetric imaging at 300 MHz using radiofrequency power saturation effects. Antioxid Redox Sign 9:1709–1716.

23. Maresch GG, Mehring M, Emid S. 1986. High-resolution electron-spin-resonance imaging. Physica B & C 138:261–263.
24. Subramanian S, Devasahayam N, Murugesan R, Yamada K, Cook J, Taube A, et al. 2002. Single-point (constant-time) imaging in radiofrequency fourier transform electron paramagnetic resonance. Magn Reson Med 48:370–379.
25. Schneiders NJ, Post H, Brunner P, Ford J, Bryan RN, Willcott MR. 1983. Accurate T2 NMR images. Med Phys 10:642–645.
26. Liu JH, Nieminen AOK, Koenig JL. 1989. Calculation of T1, T2, and proton spin-density images in nuclear magnetic-resonance imaging. J Magn Reson 85:95–110.
27. Milov AD, Pusep AY, Dzuba SA, Tsvetkov YD. 1985. Electron-spin echo as a method of electron-spin-resonance tomography. Chem Phys Lett 119:421–425.
28. Coy A, Kaplan N, Callaghan PT. 1996. Three-dimensional pulsed ESR imaging. J Magn Reson Ser A 121:201–205.
29. Blank A, Dunnam CR, Borbat PP, Freed JH. 2004. Pulsed three-dimensional electron spin resonance microscopy. Appl Phys Lett 85:5430–5432.
30. Ulrich M, Wokrina T, Drescher M, Dormann E. 2005. Comparison of 2-D ESR imaging techniques in two frequency ranges. Appl Magn Reson 29:385–399.
31. Mailer C, Sundramoorthy SV, Pelizzari CA, Halpern HJ. 2006. Spin echo spectroscopic electron paramagnetic resonance imaging. Magn Reson Med 55:904–912.
32. Epel B, Subramanian S, Mailer C, Halpern HJ. 2007. A versatile 250 MHz pulse EPR imager for in vivo oxymetry. 49th Rocky Mountain Conference on Analytic Chemistry, EPR symposia, July 22–26, Breckenridge, Colorado.
33. Anderson WA. 1961. Electrical current shims for correcting magnetic fields. Rev Sci Instrum 32:241–250.
34. Rinard GA, Quine RW, Eaton GR, Eaton SS, Barth ED, Pelizzari CA, et al. 2002. Magnet and gradient coil system for low-field EPR imaging. Concept Magn Reson 15:51–58.
35. Quine RW, Rinard GA, Eaton SS, Eaton GR. 2002. A pulsed and continuous wave 250 MHz electron paramagnetic resonance spectrometer. Concept Magn Reson 15:59–91.
36. Quine RW, Eaton GR, Dillon S. 2006. Fast-response VHF pulsed 2 KW power amplifiers. Concept Magn Reson B 29:185–190.
37. Rinard GA, Quine RW, Eaton GR, Eaton SS. 2002. 250 MHz crossed-loop electron paramagnetic resonator for pulsed resonance. Concept Magn Reson 15:37–46.
38. Epel B, Gromov I, Stoll S, Schweiger A, Goldfarb D. 2005. Spectrometer manager: a versatile control software for pulse EPR spectrometers. Concept Magn Reson B 26:36–45.
39. Ahn KH, Halpern HJ. 2007. Spatially uniform sampling in 4-D EPR spectral-spatial imaging. J Magn Reson 185:152–158.
40. Ahn KH, Halpern HJ. 2007. Comparison of local and global angular interpolation applied to spectral-spatial EPR image reconstruction. Med Phys 34: 1047–1052.
41. Owenius R, Eaton GR, Eaton SS. 2005. Frequency (250 MHz to 9.2 GHz) and viscosity dependence of electron spin relaxation of triarylmethyl radicals at room temperature. J Magn Reson 172:168–175.
42. Schweiger A, Jeschke G. 2001. Principles of Pulse Electron Paramagnetic Resonance. New York: Oxford University Press.
43. Devasahayam N, Subramanian S, Murugesan R, Hyodo F, Matsumoto KI, Mitchell JB, et al. 2007. Strategies for improved temporal and spectral resolution in in vivo oximetric imaging using time-domain EPR. Magn Reson Med 57:776–783.